

This is a repository copy of *Dehydration of Alginic Acid Cryogel by TiCl<sub>4</sub> vapor : Direct Access to Mesoporous TiO<sub>2</sub>@C Nanocomposites and Their Performance in Lithium-Ion Batteries*.

White Rose Research Online URL for this paper:

<https://eprints.whiterose.ac.uk/150818/>

Version: Accepted Version

---

## Article:

Kim, Sanghoon, De Bruyn, Mario [orcid.org/0000-0002-9687-1606](https://orcid.org/0000-0002-9687-1606), Alauzun, Johan G. et al. (7 more authors) (2019) Dehydration of Alginic Acid Cryogel by TiCl<sub>4</sub> vapor : Direct Access to Mesoporous TiO<sub>2</sub>@C Nanocomposites and Their Performance in Lithium-Ion Batteries. ChemSusChem. pp. 2660-2670. ISSN 1864-564X

<https://doi.org/10.1002/cssc.201900781>

---

## Reuse

Items deposited in White Rose Research Online are protected by copyright, with all rights reserved unless indicated otherwise. They may be downloaded and/or printed for private study, or other acts as permitted by national copyright laws. The publisher or other rights holders may allow further reproduction and re-use of the full text version. This is indicated by the licence information on the White Rose Research Online record for the item.

## Takedown

If you consider content in White Rose Research Online to be in breach of UK law, please notify us by emailing [eprints@whiterose.ac.uk](mailto:eprints@whiterose.ac.uk) including the URL of the record and the reason for the withdrawal request.

# Dehydration of alginic acid cryogel by $\text{TiCl}_4$ vapor: a direct access to mesoporous $\text{TiO}_2@\text{C}$ nanocomposites and their performance in lithium ion batteries

Sanghoon Kim,<sup>[a]</sup> Mario De bruyn,<sup>[b]</sup> Johan G. Alauzun,<sup>[a]</sup> Nicolas Louvain,<sup>[a,c]</sup> Nicolas Brun,<sup>[a]</sup> Duncan J. Macquarrie,<sup>[b]</sup> Lorenzo Stievano,<sup>[a,c]</sup> P. Hubert Mutin,<sup>[a]</sup> Laure Monconduit,<sup>\*,[a,c]</sup> and Bruno Boury,<sup>\*,[a]</sup>

**Abstract:** A new strategy for the synthesis of mesoporous  $\text{TiO}_2@\text{C}$  nanocomposites via the direct mineralization of seaweed derived-alginic acid cryogel by  $\text{TiCl}_4$  through a solid/vapour reaction pathway was developed. In this synthesis, alginic acid cryogel can act multiple roles: i) mesoporous template, ii) carbon sources, and also iii) oxygen source for the  $\text{TiO}_2$  precursor,  $\text{TiCl}_4$ . The resulting  $\text{TiO}_2@\text{alginic acid}$  composite was then transformed either into pure mesoporous  $\text{TiO}_2$  by calcination, or into mesoporous  $\text{TiO}_2@\text{C}$  nanocomposites by pyrolysis. By comparing with a non-porous  $\text{TiO}_2@\text{C}$  composite, the importance of mesopore in the performance of electrodes for lithium ion batteries based on mesoporous  $\text{TiO}_2@\text{C}$  composite is clearly evidenced. In addition, the carbon matrix in the mesoporous  $\text{TiO}_2@\text{C}$  nanocomposite also show electrochemical activity vs. lithium ions, providing twice the capacity of pure mesoporous  $\text{TiO}_2$  or alginic acid derived mesoporous carbon (A600). Given the simplicity and environment friendliness of the process, the mesoporous  $\text{TiO}_2@\text{C}$  nanocomposite could greatly satisfy the main prerequisites of green and sustainable chemistry, while showing improved electrochemical performance as negative electrode for lithium ion batteries.

## Introduction

The demand for enhanced electrochemical energy storage devices such as portable electronic devices or hybrid electric vehicles is ever increasing.<sup>[1],[2]</sup> This stimulates the search for more sustainable processing of the required materials, better respecting the Green Chemistry Principles. Metal oxides ( $\text{M}_x\text{O}_y$ ) and  $\text{M}_x\text{O}_y@\text{C}$  composites are among such required materials<sup>[3-5]</sup> and many efforts have been devoted to the fine tailoring of hierarchical macro- to microporous structures with tailored controlled porosity,<sup>[6],[7]</sup> doping,<sup>[8],[9]</sup> particle size<sup>[10-12]</sup> and structure.<sup>[13],[14]</sup> In this context, biomass polymers such as lignin or polysaccharides as C-source or bio-templates are intensively

explored as starting reagents for the processing of nanostructured C,  $\text{M}_x\text{O}_y$  and  $\text{M}_x\text{O}_y@\text{C}$  composites for applications in clean and efficient energy production and storage.<sup>[11],[15-19]</sup>

To process the material, atomic layer deposition<sup>[20-22]</sup> or chemical vapor decomposition<sup>[23,24]</sup> are not competitive with solution processing that offers better productivity, safety and simplicity. Sol-gel, hydrothermal and solvothermal processes have been extensively and sometime successfully used with soluble (starch, alginic acid, lignin) or insoluble (cellulose) biopolymers.<sup>[3],[25-27]</sup>

This represents one of the basic idea of the Extreme Biomimetic approach, a special field in bioinspired materials science, which includes all types of hydrothermal synthesis as well as all the new way to assemble bio-template with synthetic material, by in vivo or in vitro reactions.<sup>[28]</sup> For example, the extreme biomimetic was used to obtain and describe rare examples of the assembly and binding between protein and metals such as  $\text{Cu}(0)$  or  $\text{Fe}(0)$ .<sup>[29]</sup> A unique structure was obtained with chitin as scaffold for  $\text{ZrO}_2/\text{chitin}$  nanoassembly<sup>[30,31]</sup> with the application for supercapacitors.<sup>[32]</sup> Spongin is another attractive material to prepare  $\text{MnO}_2/\text{C}$ <sup>[33]</sup> or  $\text{TiO}_2/\text{Spongin}$  material<sup>[34]</sup> for electrochemical application or depollution, respectively. However, cellulose is so far the most widely used template for such approach, as both carbon source and template in the preparation of nanocomposite such as  $\text{Ag}@\text{TiO}_2/\text{C}$ <sup>[35,36]</sup> or  $\text{SnO}_2/\text{C}$ <sup>[37]</sup> as negative electrode material for lithium ion batteries. Recently, the use of alginic acid has been developed in sol-gel templated process to elaborate porous metal oxide-based catalyst.<sup>[38,39]</sup> In terms of Green Chemistry, these processes present some drawbacks using water or solvents, sometimes high temperatures ( $>100^\circ\text{C}$ ) and reagents requiring synthetic and purification steps from the cheapest metal chloride,  $\text{TiCl}_4$  in the case of Ti-based metal oxides.<sup>[40]</sup>

We recently disclosed an innovative process based on the direct reaction a cellulosic biomass such as cotton, filter paper, or nanofibrillated cellulose with the simplest and cheapest metal oxide precursors.<sup>[17],[41-43]</sup> In such reactions, the biomass is not only considered as a template, but also as a reagent, from which O atoms are transferred to the metal precursors, in full agreement with the Green Chemistry principle of economy of atoms. The dehydration of the polysaccharides is the main chemical transformation occurring during the process and the resulting materials can then be converted into metal oxides by calcination or into their composites with carbon by pyrolysis.

Our interest in applying this treatment to alginic acid (AA) results from the high performances of the mesoporous AA-derived carbon and titanate composites we recently introduced in the field of lithium ion batteries (LIB).<sup>[11],[44]</sup> It is well-known that titanium-based materials are among the best promising candidates as negative electrodes alternative to carbonaceous materials (e.g.,

- [a] Dr. S. Kim, Dr. J. G. Alauzun, Dr. N. Louvain, Dr. N. Brun, Pr. L. Stievano, Dr. P. M. Mutin, Dr. L. Monconduit,\* B. Boury,\* Institut Charles Gerhardt Montpellier, UMR 5253 Univ. Montpellier-CNRS-ENSCM, Montpellier, France  
E-mail: laure.monconduit@umontpellier.fr, bruno.boury@umontpellier.fr
- [b] Dr. M. De bruyn, Dr. Duncan J. Macquarrie  
Green Chemistry Centre of Excellence, University of York, York, North Yorkshire, YO10, 5DD, UK
- [c] Dr. N. Louvain, Pr. L. Stievano, Dr. L. Monconduit  
Réseau sur le Stockage Electrochimique de l'Energie (RS2E), CNRS, FR3459, 33 Rue Saint Leu, 80039 Amiens Cedex, France

Supporting information for this article is given via a link at the end of the document.

## FULL PAPER

graphite), owing to their good theoretical specific capacity, low cost, safety and environmental friendliness.<sup>[44],[45]</sup> However, the practical application of these materials is greatly hampered by their poor electronic conductivity and slow lithium-ion kinetics, which further limit their rate capability, as in the case of anatase  $\text{TiO}_2$ .<sup>[46]</sup> To improve the electronic conductivity, carbon coating<sup>[47],[48]</sup> or heteroatom doping have been proposed.<sup>[49],[50]</sup> Concerning lithium-ion kinetics, nano-structuring of  $\text{TiO}_2$  with controlled porosity could be a substantial solution as it can provide a larger contact area between electrode and electrolyte, resulting in an enhancement of lithium-ion diffusion inside the electrode.<sup>[51]</sup> Accordingly, research has increasingly focused on the design of porous  $\text{TiO}_2$ @C nanocomposites, where fast lithium ion diffusion in the mesopores and an enhanced conductivity ensured by the carbon matrix improve the electrochemical performance. This was obtained using various biopolymers as both templates and C-precursors via a hydrolytic sol-gel process.<sup>[17],[41]</sup>

In this work, the synthesis of  $\text{TiO}_2$ @C nanocomposites by the direct mineralization of AA by  $\text{TiCl}_4(\text{g})$ , a cheaper and solvent-free approach, is presented. This is expected to produce a chemical modification of the AA before pyrolysis, and consequently to a significantly different carbon from that obtained by direct pyrolysis of non-mineralized AA. Moreover, only few papers discuss about the advantages of lithium ion insertion into both  $\text{TiO}_2$  (2.5 to 1.0 V vs  $\text{Li}^+/\text{Li}$ ) (or even other metal oxides such as  $\text{Li}_4\text{Ti}_5\text{O}_{12}$ : 2.5 to 1.2 V vs  $\text{Li}^+/\text{Li}$ ) and carbon (below 1.0 V vs  $\text{Li}^+/\text{Li}$ ) in such C-rich composites.<sup>[52-54]</sup> Therefore, our  $\text{TiO}_2$ @C nanocomposites were investigated in a large range of potential (from 3 to 0 V) to take advantage of the reversible storage of lithium ions in both  $\text{TiO}_2$  and carbon, which could improve the electrochemical performance, such as higher capacity than  $\text{TiO}_2$  or carbon investigated separately.

Here, the synthesis of mesoporous  $\text{TiO}_2$ @C nanocomposites starts by a direct mineralization of seaweed derived-alginic acid cryogel (CG) by  $\text{TiCl}_4$  via solid/vapor reaction pathway (Fig. 1) giving hybrid composite so-called  $\text{TiO}_2$ @CG, then transformed into mesoporous anatase  $\text{TiO}_2$  (CG- $\text{TiO}_2$ ) by calcination or into a mesoporous  $\text{TiO}_2$ @C nanocomposite (CG- $\text{TiO}_2$ @C) by pyrolysis. For comparison, we also performed the same experiment with a powder of alginic acid (P) leading to P- $\text{TiO}_2$  or P- $\text{TiO}_2$ @C composite from the  $\text{TiO}_2$ @P intermediate hydride. Very clear differences are evidenced, showing the advantages of the cryogel substrate and the formation of a mesoporous carbon-containing composite as electrode materials for LIB. We stress that the carbon part in the mesoporous  $\text{TiO}_2$ @C composite could not only provide a rigid support for  $\text{TiO}_2$  by ensuring its stability during electrochemical cycling, but also create a conductive part, resulting in the improvement of its high rate capability. In addition, this carbon matrix can act as electrochemical active material vs lithium ion, leading to twice the capacity of porous  $\text{TiO}_2$  or alginic acid derived mesoporous carbon (A600) alone.

The AA in this study is approximately 61% mannuronic acid and 39% guluronic acid with an average molecular weight of approximately 240 kDa.<sup>1</sup> It was dissolved in water to prepare a mesoporous cryogel, with a specific surface area of  $190 \text{ m}^2 \text{ g}^{-1}$  and a pore volume of  $1.24 \text{ cm}^3 \text{ g}^{-1}$ .<sup>[55]</sup> To maintain such a mesoporosity of the AA gel during freeze-drying, tert-butyl alcohol is added to form the water/tert-butyl alcohol eutectic (approximately 67/33), otherwise, the mesoporous network collapses, yielding cryogel with a pore volume of only ca.  $0.3 \text{ cm}^3 \text{ g}^{-1}$ . The TGA analysis of the CG evidenced the hydration of alginic acid at temperatures above  $100^\circ\text{C}$ ,<sup>[56]</sup> and no weight loss below such temperature. Such CG was then directly reacted with  $\text{TiCl}_4$  in an autoclave under autogenous pressure at  $80^\circ\text{C}$ . At this temperature, Titanium(IV) chloride (Bp.  $136.4^\circ\text{C}$  at  $101 \text{ } 10^3 \text{ Pa}$ ) has a vapor pressure close to  $25 \text{ } 10^3 \text{ Pa}$  in open vessel. Consequently,  $\text{TiCl}_4$  is only partly gaseous at the beginning of the reaction, a liquid/gas equilibrium is maintained through the reaction with the cryogel.

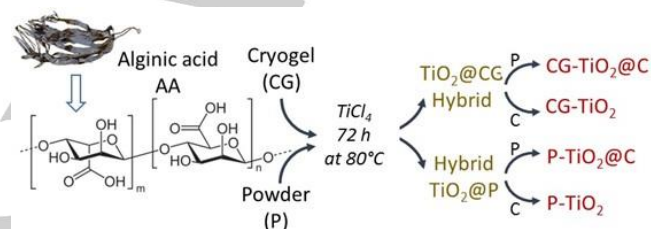


Fig. 1. Schematic representation of the synthesis of  $\text{TiO}_2$ @C and  $\text{TiO}_2$  samples.

The modification of the AA is evidenced by  $^{13}\text{C}$  Solid State NMR spectroscopy only by a difference in the relative intensity of several signals like that of the carboxylic group G6+M6 at 170.1 ppm and the anomeric carbon G1+M1 at 104.2 ppm (G relates to the Guluronic units while M refers to the Mannuronic units).<sup>[57]</sup> The broadness of the signal doesn't allow one to identify whether the mannuronic units are more or less impacted than the guluronic. Unlike cellulose,<sup>[42]</sup> the formation of aromatic compounds (e.g. furans or arenes) during the reductive dehydration of AA by  $\text{TiCl}_4$  vapor wasn't evidenced. A possible reason is that for AA, dehydration can lead to ester or anhydride functions with chemical shifts close to the ones of carboxylic and alcohol functions.

## Results and Discussion

### Synthesis and characterization of mesoporous $\text{TiO}_2$ @C, $\text{TiO}_2$ and A600 materials



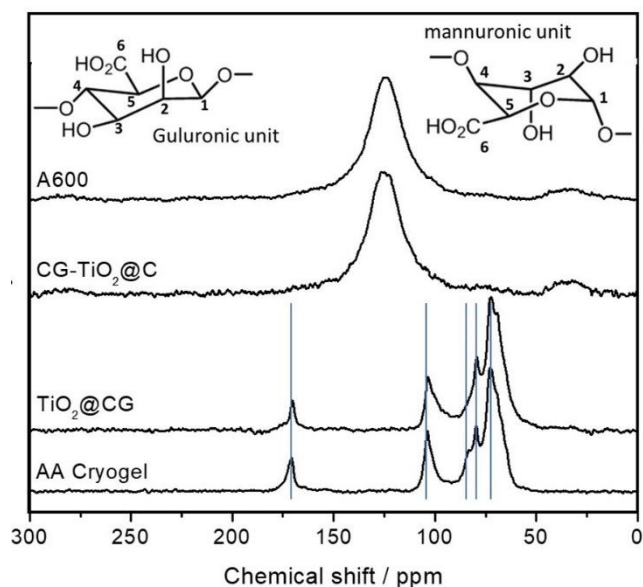


**Fig. 2.** CPMAS  $^{13}\text{C}$  SS NMR images of a) CG, b)  $\text{TiO}_2\text{@CG}$ , c)  $\text{CG-TiO}_2\text{@C}$  and d) A600.

The hybrid composites were then pyrolyzed or calcined at  $600^\circ\text{C}$  giving respectively  $\text{TiO}_2\text{@C}$  composites or pure  $\text{TiO}_2$  (see Fig. 1). A sample of CG-derived carbon (A600) was also obtained by direct pyrolysis at  $600^\circ\text{C}$  of GC in order to highlight the possible effect of the  $\text{TiCl}_4$  on AA and its consequences on the formation of the carbonaceous residue in  $\text{CG-TiO}_2\text{@C}$ .

TGA analyses in air of the material before thermal treatment of  $\text{TiO}_2\text{@CG}$  and  $\text{TiO}_2\text{@P}$  lead to a weight loss of 65.8% at  $1000^\circ\text{C}$ , the weight loss of CG in the same conditions being of 99.1%. Consequently, the mass of  $\text{TiO}_2$  in these material is around 34.8 %. On sample obtained after pyrolysis, a TGA in air of  $\text{CG-TiO}_2\text{@C}$  (Fig. S1 and see Fig. S2 for the others) allows to evaluate the C-content to  $\sim 33.7$  wt%,  $\text{TiO}_2$  being the major component  $\sim 67.3$  wt%. The same analysis on  $\text{P-TiO}_2\text{@C}$  gives: C-content 39.9 w% C and  $\text{TiO}_2$  60.1 wt%.

The elemental mapping obtained by EDX indicates a perfectly homogeneous distribution of Ti, O and C in  $\text{GC-TiO}_2\text{@C}$  and no segregation at the nanometer level (Fig. S3) whereas the segregation in two phases ( $\text{TiO}_2$  and C) is clearly observed for  $\text{P-TiO}_2\text{@C}$  (Fig. S4). The quantitative analysis of  $\text{CG-TiO}_2\text{@C}$ , assuming 2 O atoms for each Ti atom, lead to an atomic C/O ratio  $\sim 23$ -24 in the carbonaceous part of the composite. This must be compared to that of A600: C/O atomic ratio is  $\sim 14.0$  (Table 1). On one hand, this much lower C/O ratio suggests that A600 is hardly graphitized or should be largely amorphous at this temperature. On the other hand, the high C/O ratio in  $\text{CG-TiO}_2\text{@C}$  agrees with the role of AA as O-donor.

The morphology of  $\text{CG-TiO}_2\text{@C}$  investigated by SEM is very similar to the one of A600 (Fig. 3a) and CG (Fig. 3c). The large particles observed at low magnification ( $\sim 10$ - $30\ \mu\text{m}$ ) appeared as a dense packing of disordered meso-to-macro worm-like sub-structure at higher magnification.

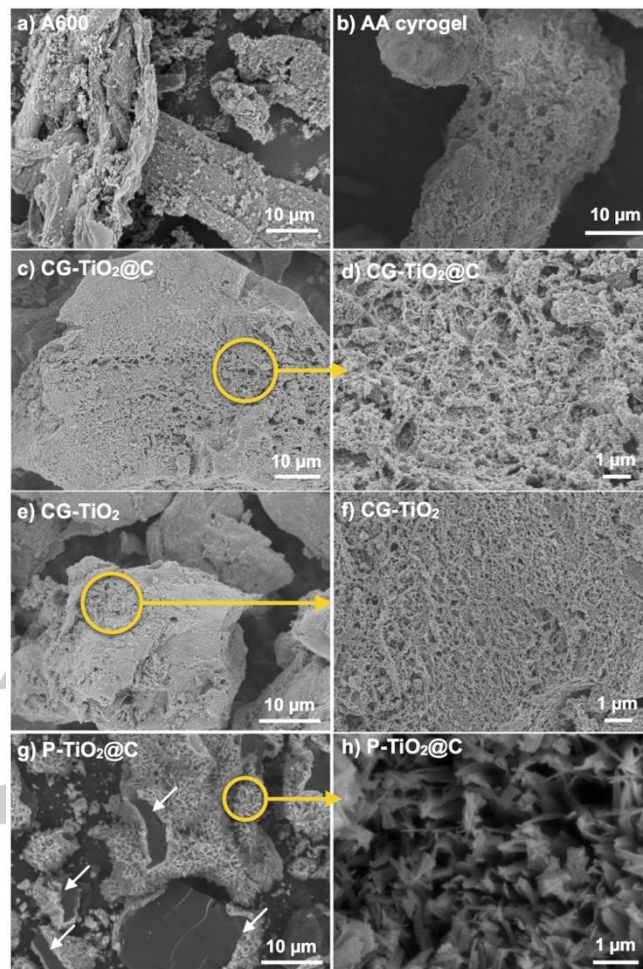


**Fig. 3.** SEM images of a-b) A600, b) alginate acid (AA) cryogel, c-d)  $\text{CG-TiO}_2\text{@C}$ , e-f)  $\text{CG-TiO}_2$ , g-h)  $\text{P-TiO}_2\text{@C}$  and f)  $\text{P-TiO}_2\text{@C}$ . Backscattered electrons detector used for  $\text{P-TiO}_2\text{@C}$  sample.

This type of morphology is also the one of A600 (Fig. 3a). It thus appears that the reaction between  $\text{TiCl}_4$  and alginate acid perfectly kept the initial CG morphology, which is then preserved upon pyrolysis. At the highest magnification ( $\times 10000$ ) (Fig. 3d), the porous structure is clearly visible. The morphology of  $\text{CG-TiO}_2$  is very similar to that of  $\text{CG-TiO}_2\text{@C}$  (Fig. 3e) but the surface seems smoother at high magnification (Fig. 3f), a probable effect of the removal of organic matters by calcination. Since this material is now pure  $\text{TiO}_2$ , the templating role of CG at the nanometer level is demonstrated. Comparatively, the morphology of  $\text{P-TiO}_2\text{@C}$  is completely different: the segregation in two separated phases,  $\text{TiO}_2$  and carbon, is clearly observed (as specified by white arrows in Fig. 3g). In this case, the treatment of P by  $\text{TiCl}_4$  leads to a crust ( $\sim 0.5$  -  $2\ \mu\text{m}$  thick) of flattened  $\text{TiO}_2$  fibers a few microns long surrounding the surface of the AA grains ( $> 10\ \mu\text{m}$ ), as similar to  $\text{TiO}_2$  obtained through the conventional non-hydrolytic sol-gel method.<sup>[58]</sup>

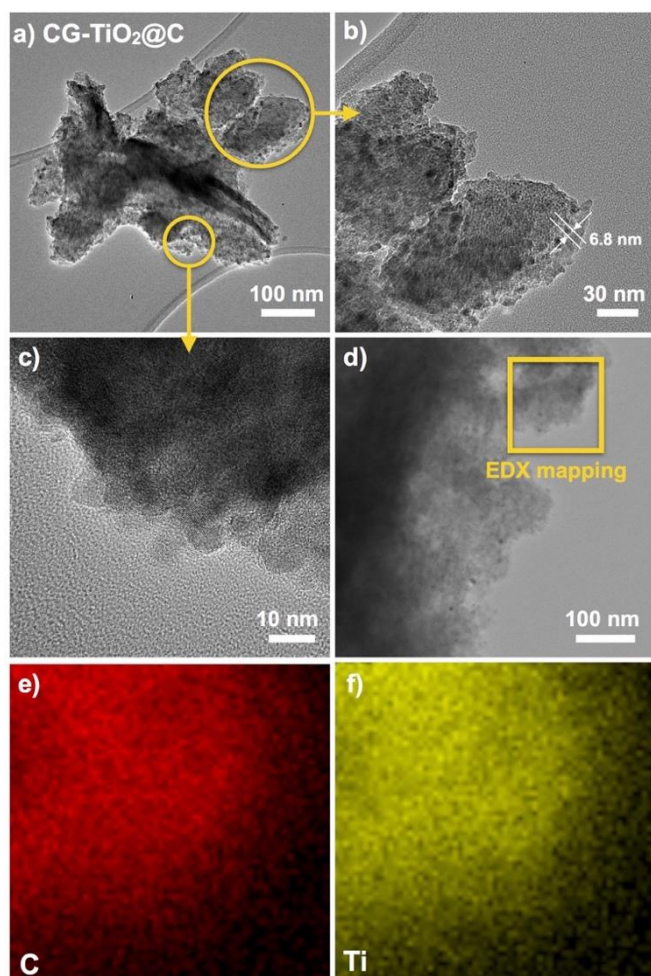


**Fig. 4.** a-c) TEM images, d) STEM image and e-f) EDX mapping of CG-TiO<sub>2</sub>@C.

TEM (Fig. 4a-c) of CG-TiO<sub>2</sub>@C reveal the presence of TiO<sub>2</sub> nanoparticles ( $6.8 \pm 1.2$  nm, counting 20 particles) closely assembled and embedded into a carbon matrix. No fibres, needles or flakes of TiO<sub>2</sub> were observed. TEM-EDX mapping (Fig. 4d-f) reveals that both carbon and TiO<sub>2</sub> particles are homogeneously dispersed with no segregation. In case of A600 (Fig. S5), TEM confirms that the mesoporosity arises from the entanglement of bundles of alginic acid chains (with the thickness of  $\sim 15$  nm)<sup>[59]</sup> present in the cryogel and maintained during carbonization.

The Raman spectra of samples before thermal treatment do not present any signals clear and strong enough to be interpretable. This is significantly different from the one obtained with cellulose, as reported previously.<sup>[40]</sup> The same analyses performed on the pyrolyzed samples CG-TiO<sub>2</sub>@C and CG-TiO<sub>2</sub> show an intense band at  $148\text{ cm}^{-1}$  and weaker bands at  $394$ ,  $512$  and  $639\text{ cm}^{-1}$  attributed to the characteristic modes of anatase TiO<sub>2</sub> (Fig. 5a).<sup>[60]</sup> The peak shift, especially for  $E_{g(1)}$  mode of CG-TiO<sub>2</sub>@C compared to CG-TiO<sub>2</sub>, might indicate formation of intimately mixed TiO<sub>2</sub> and C species as observed in the case of TiO<sub>2</sub>/graphene oxide composites.<sup>[61]</sup> In the higher range of  $1000$  to  $2000\text{ cm}^{-1}$  (Fig. S6), both in-plane vibration of disordered amorphous carbon band (D-

band) at  $1337\text{ cm}^{-1}$  and crystalline graphitic carbon band (G-band) at  $1585\text{ cm}^{-1}$  are observed for CG-TiO<sub>2</sub>@C and A600 with the  $I_D/I_G$  ratios estimated to  $0.9$ - $1.0$  in both cases. Based on the width of these bands and the low  $I_D/I_G$ , the carbon has a low degree of graphitization, even for A600, as a result of the low temperature of carbonization ( $600^\circ\text{C}$ ).

Before any thermal treatment, XRD analyses in Figure 5b show peaks at  $2\theta = 15.6$ ,  $20.6^\circ$  indicating a partial preservation of crystalline AA. However, the broadening of these signals compared to the pristine AA cryogel and the absence of other peaks, notably the one at  $2\theta = 13.3^\circ$ , suggest an important decrease of the crystallinity. In such TiO<sub>2</sub>@CG sample, very poorly crystallized anatase might be considered on the basis of the broad signals at  $2\theta = 25.3$  and  $48.1$  corresponding to (101) and (200) reflections. For samples after thermal treatment, CG-TiO<sub>2</sub>@C or CG-TiO<sub>2</sub>, the diffraction peaks of anatase TiO<sub>2</sub> (JCPDS Card no. 21-1272) are observed at  $2\theta = 25.3$ ,  $38.3$ ,  $48.1$ ,  $54.1$ ,  $55.0$  and  $62.6^\circ$ , corresponding to the (101), (004), (200), (105), (211) and (204) reflections, respectively. The size of TiO<sub>2</sub> crystallites estimated by the Scherrer equation on the (101) peak is  $\approx 6$  nm and  $\approx 15$  nm for CG-TiO<sub>2</sub>@C and CG-TiO<sub>2</sub>, respectively. As frequently reported, the carbon in CG-TiO<sub>2</sub>@C effectively limits the growth of the TiO<sub>2</sub> crystallites during calcination. For samples before or after thermal treatment, no characteristic peaks for carbon were observed either for CG-TiO<sub>2</sub>@C or TiO<sub>2</sub>@GC, demonstrating that carbon in these composites is largely amorphous. For comparison, broad signals of amorphous carbon are observed for A600 at around  $22^\circ$  and  $42^\circ$ .



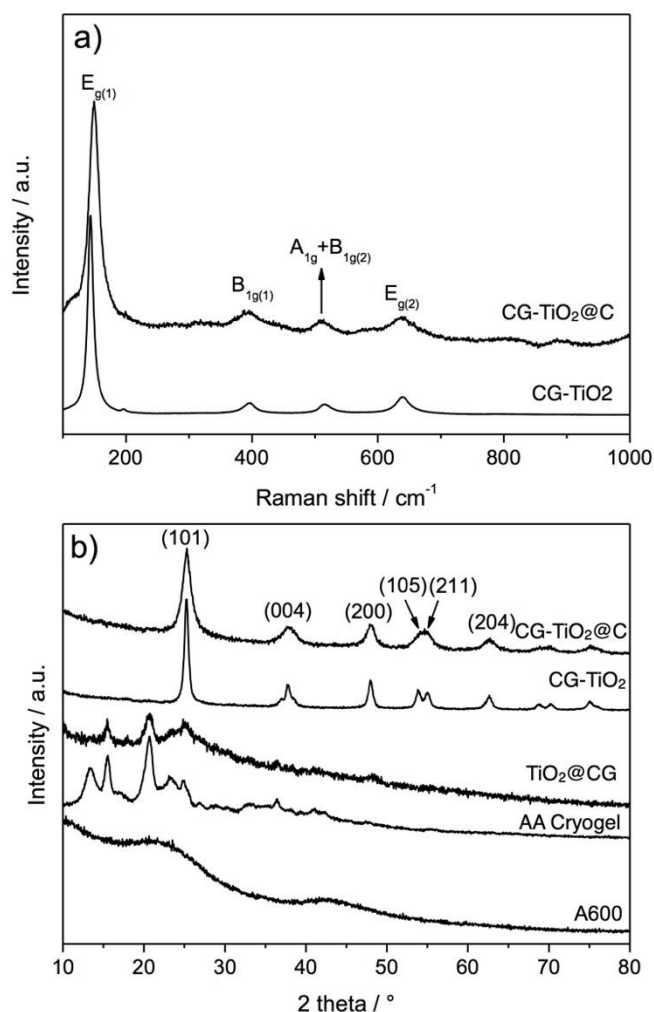


**Fig. 5.** a) Raman spectra of CG-TiO<sub>2</sub>@C and CG-TiO<sub>2</sub> (100 to 1000 cm<sup>-1</sup>) b) X-ray powder diffraction patterns of CG-TiO<sub>2</sub>@C and CG-TiO<sub>2</sub>, TiO<sub>2</sub>@CG, AA Cryogel and A600.

The textural properties evaluated by N<sub>2</sub> physisorption measurements show that CG-TiO<sub>2</sub>@C and CG-TiO<sub>2</sub> are essentially mesoporous, with a large pore size distribution in the range 2 - 50 nm (Fig. S7 and Table 1). The BET surface area and the total pore volume of CG-TiO<sub>2</sub>@C, CG-TiO<sub>2</sub> were calculated to be 394 m<sup>2</sup> g<sup>-1</sup>, 54 m<sup>2</sup> g<sup>-1</sup> and 0.47 cm<sup>3</sup> g<sup>-1</sup>, 0.34 cm<sup>3</sup> g<sup>-1</sup>, respectively. At the opposite, P-TiO<sub>2</sub>@C and P-TiO<sub>2</sub>, synthesized using P-AA, are clearly non-porous with negligible pore volumes (Fig. S7). Besides, a direct carbonization of the AA cryogel leads to the highly porous carbonaceous A600, with a pore volume of 1.04 cm<sup>3</sup> g<sup>-1</sup>. The last line of the Table 1 are the values corresponding to a hypothetic mixture of 67 wt% of GC-TiO<sub>2</sub> and 33 wt% of A600, the proportion of C and TiO<sub>2</sub> found for the composite GC-TiO<sub>2</sub>@C. By comparison, CG-TiO<sub>2</sub>@C has a much higher specific surface area (+90%), but a lower mesoporosity. This might be the effect of the TiCl<sub>4</sub> treatment, but also of the confinement of the alginate acid by TiO<sub>2</sub>.

**Table 1.** Textural properties of TiO<sub>2</sub>@C composite, TiO<sub>2</sub> and A600 materials

Sample	S <sub>BET</sub> [a]	PV <sub>total</sub> [b]	PV <sub>&lt;100 nm</sub> [c]	PV <sub>micro</sub> [d]	C:O [e]
CG-TiO <sub>2</sub> @C	394	0.47	0.45	0.14	23.6
CG-TiO <sub>2</sub>	54	0.34	0.33	< 0.01	-
P-TiO <sub>2</sub> @C	214	0.09	0.09	0.08	-
P-TiO <sub>2</sub>	13	0.05	0.05	< 0.01	-
A600	514	1.12	1.06	0.22	14.0
(67% CG-TiO <sub>2</sub> + 33% A600)	205	0.58	0.61	0.11	-

[a] Surface area determined by BET method (m<sup>2</sup> g<sup>-1</sup>). [b] Total pore volume at P/P<sub>0</sub> = 0.99 (cm<sup>3</sup> g<sup>-1</sup>). [c] Pore volume less than 100 nm calculated by DFT method (cm<sup>3</sup> g<sup>-1</sup>). [d] Micropore volume calculated by DFT method (cm<sup>3</sup> g<sup>-1</sup>). [e] C:O atomic ratio obtained by SEM-EDX; For CG-TiO<sub>2</sub>@C, C:O ratio was calculated by subtraction of oxygen of TiO<sub>2</sub>; For P-TiO<sub>2</sub>@C, C:O ratio was not calculated as the distribution of carbon is not homogenous. (See Fig. 3 and Fig. S4 for SEM images).

The above data indicate a strong modification of AA upon treatment with TiCl<sub>4</sub> at low temperature. Among different possible reactions, the most likely is the TiCl<sub>4</sub> vapor diffusion inside the AA cryogel and its reactions with the hydroxyl and acidic functions leading to the formation of [Ti-O-C]-containing species and the concomitant release of HCl(g). Their reaction by Ti-Cl/C-O bond exchange may lead to the formation of TiO<sub>2</sub> according to a Non-hydrolytic Sol-Gel reaction path.<sup>[57]</sup> The strongly acidic HCl vapour is also able to promote the intra- or intermolecular dehydration of AA with concomitant formation of esters, anhydrides and unsaturated functions. The water released *in situ* then can react with any [Ti-Cl]-containing species and progressively leads to TiO<sub>2</sub>. This corresponds well to the O-donor role of AA. Besides, the growth of TiO<sub>2</sub> is perfectly templated by AA and leads to a controlled nano-composite. Finally, the modification of AA by TiCl<sub>4</sub> ultimately leads, after pyrolysis, to a carbon with a different C:O ratio from that resulting from the direct pyrolysis of untreated AA. Anatase rutile phase transition is not observed here during the thermal treatment. The exact transition temperature strongly depending on the particle size or the synthesis method.<sup>[62]</sup> In our case, no rutile phase was observed by XRD, probably because of the nanosize of the TiO<sub>2</sub> anatase particles (6.8 nm), which become significantly resistant against phase transition.<sup>[63]</sup> In addition, the pyrolysis generates carbonaceous char which part of them deposit on the TiO<sub>2</sub> particles and inhibit their crystal growth and crystallization.

#### Electrochemical investigation as lithium ion batteries electrode

The lithium ion storage properties of CG-TiO<sub>2</sub>@C, CG-TiO<sub>2</sub> and A600 were evaluated by galvanostatic discharge-charge measurement at different current densities. To facilitate the comparison of the different materials, their capacities were calculated based on the total mass of electrode material, not on that of TiO<sub>2</sub> only.

As shown in Fig 6b, CG-TiO<sub>2</sub> shows the typical charge/discharge galvanostatic profile of anatase TiO<sub>2</sub> with three difference potential regions; i) a rapid drop to 1.8 V representing the formation of a solid solution of Li<sub>x</sub>TiO<sub>2</sub>, ii) a plateau around 1.8 V ascribed to the two-phase reaction between tetragonal Li<sub>x</sub>TiO<sub>2</sub>

## FULL PAPER

and orthorhombic lithium titanate  $\text{Li}_{0.5\pm0}\text{TiO}_2$ , and finally iii) another two-phase reaction until 1.0 V leading to rock-salt tetragonal  $\text{LiTiO}_2$ .<sup>[51]</sup> The shape of the plateau at 1.8 V is strongly dependent on the particle size of  $\text{TiO}_2$ : a smaller particle size corresponds to a shorter plateau. Conversely, the extent of the sloping region from 1.8 V to 1.0 V, attributed to reversible surface lithium storage, is directly proportional to the specific surface area and the porosity, and large surface areas can largely increase the overall capacity.<sup>[51]</sup> The first discharge capacity of  $345 \text{ mAh g}^{-1}$  rapidly drops to  $205 \text{ mAh g}^{-1}$  at the second cycle. The corresponding large irreversible capacity can be explained by the formation of a passivation layer, a so-called solid-electrolyte interphase (SEI) during the first cycle. The capacity of CG- $\text{TiO}_2$  further drops to  $100 \text{ mA g}^{-1}$  after 10 cycles, with a capacity retention of only 78 % compared to its initial capacity ( $161 \text{ mA g}^{-1}$ ).

In case of CG- $\text{TiO}_2\text{@C}$  (Fig. 6a), the characteristic plateau of anatase is much shorter than that of CG- $\text{TiO}_2$ , due to low  $\text{TiO}_2$  content in the composite, and a long tail-like slope is observed below 1.0 V. The first and the second discharge capacity are  $1056$  and  $589 \text{ mAh g}^{-1}$ , respectively. Indeed, this tail-like galvanostatic profile below 1.0 V is characteristic of lithium insertion in hard carbon, as confirmed by electrochemical signature of A600.

For A600 (Fig. 6c), the first and the second discharge capacity are  $789$  and  $405 \text{ mAh g}^{-1}$ , respectively. The initial coulombic efficiency is 56 %, 59 % and 51 % for CG- $\text{TiO}_2\text{@C}$ , CG- $\text{TiO}_2$  and A600. The low coulombic efficiency of CG- $\text{TiO}_2\text{@C}$  compared to CG- $\text{TiO}_2$  could be due to the carbon matrix in the composite, in analogy with that of A600 (Table S1).

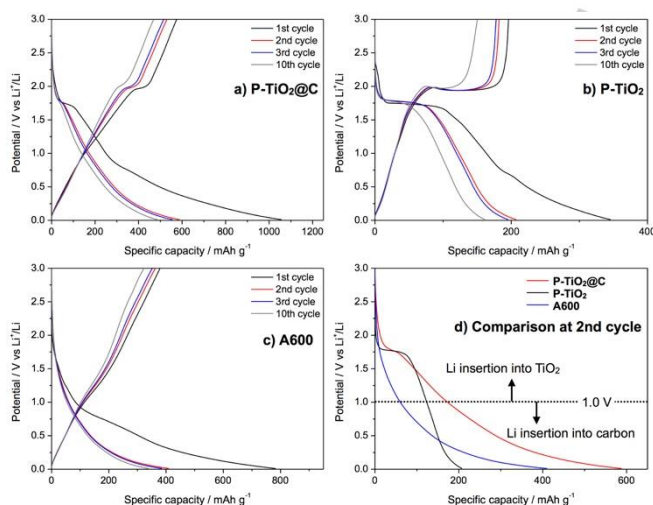
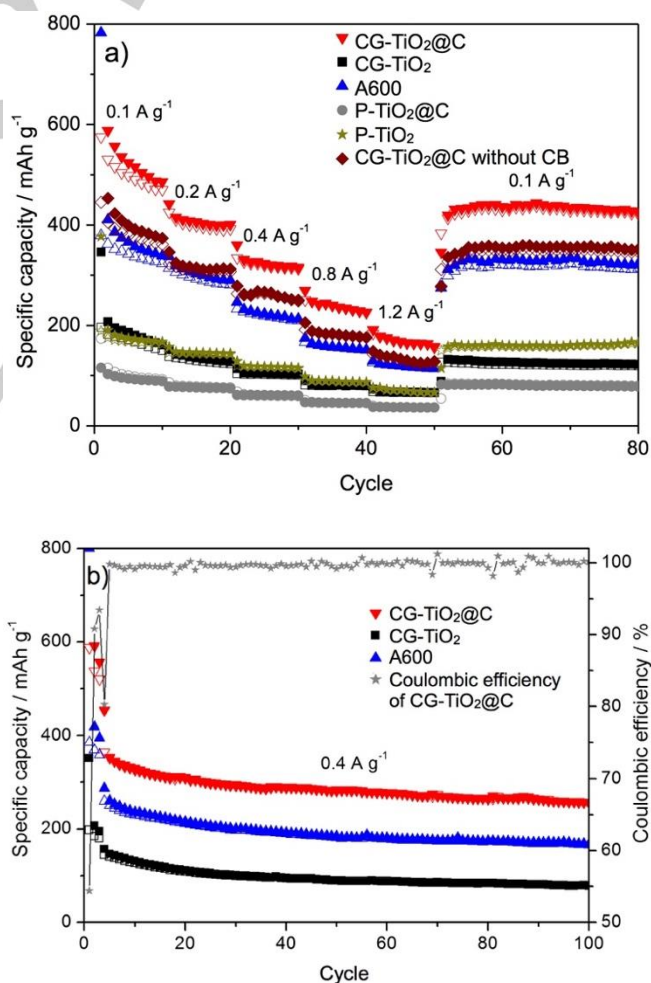


**Fig. 6.** Galvanostatic discharge-charge profile for a) CG- $\text{TiO}_2\text{@C}$ , b) CG- $\text{TiO}_2$ , c) A600 and d) comparison of the 2nd discharge at  $100 \text{ mA g}^{-1}$ .

Fig. 6d compares the second discharge of the different electrodes. As the reversible insertion-disinsertion of lithium in  $\text{TiO}_2$  mostly occurs between 1.0 and 3.0 V, whereas lithium insertion in hard carbon is reported below ca. 1.0 V (here, below ca. 1.5 V for A600), the discharge capacity of CG- $\text{TiO}_2\text{@C}$  can be roughly decomposed into two contributions. Evidently, the increase in capacity for CG- $\text{TiO}_2\text{@C}$  arises from the region below 1.0 V, attributed to the carbon contribution. Interestingly, the second

discharge capacity of CG- $\text{TiO}_2\text{@C}$  ( $589 \text{ mAh g}^{-1}$ ) is obviously higher than the simple sum ( $272 \text{ mAh g}^{-1}$ ) of the expected contributions of CG- $\text{TiO}_2$  ( $205 \text{ mAh g}^{-1} \times 66 \% = 135 \text{ mAh g}^{-1}$ ) and A600 ( $405 \text{ mAh g}^{-1} \times 66 \% = 137 \text{ mAh g}^{-1}$ ). Moreover, the specific capacity of  $\text{TiO}_2$  (calculated from the weight of  $\text{TiO}_2$ ) corresponding to the plateau at 1.8 V for both CG- $\text{TiO}_2$  ( $58 \text{ mAh g}^{-1}$  of  $\text{TiO}_2$ ) and CG- $\text{TiO}_2\text{@C}$  ( $50 \text{ mAh g}^{-1}$  of  $\text{TiO}_2$ ) is very similar. Based on these results, the difference in capacity must thus arise from the difference in the carbon contribution, which might be connected to the different nature of the two carbon matrices, as explained in the previous section (carbon in CG- $\text{TiO}_2\text{@C}$  has higher oxygen content than A600, cf. Table 1), which might interfere with lithium insertion into the carbon matrix.

Fig 7a compares the rate capability of CG- $\text{TiO}_2\text{@C}$ , CG- $\text{TiO}_2$  and A600 at various current densities from  $0.1 \text{ A g}^{-1}$  to  $1.2 \text{ A g}^{-1}$ . The most remarkable point is that the capacity of CG- $\text{TiO}_2\text{@C}$  is higher than any other samples at all current densities, for example, giving  $329 \text{ mAh g}^{-1}$  vs  $252 \text{ mAh g}^{-1}$  for CG- $\text{TiO}_2\text{@C}$  vs A600, respectively. More importantly, CG- $\text{TiO}_2\text{@C}$  recovers 94 % ( $444 \text{ mAh g}^{-1}$ ) of its pristine capacity when the current density is set back to  $0.1 \text{ A g}^{-1}$ , then becomes almost stable for 30 subsequent cycles, with a coulombic efficiency exceeding 99.0 %.



## FULL PAPER

**Fig. 7.** Rate capability and b) long-term cyclability of different TiO<sub>2</sub>@C, TiO<sub>2</sub> and A600 electrodes.

In addition, the importance of porosity and homogenous dispersion of TiO<sub>2</sub> in CG-TiO<sub>2</sub>@C or CG-TiO<sub>2</sub> can be elucidated by comparing them with non-porous P-TiO<sub>2</sub>@C or P-TiO<sub>2</sub> (Fig. 6a). For example, P-TiO<sub>2</sub>@C delivers 4 times less capacity than CG-TiO<sub>2</sub>@C at 0.1 A g<sup>-1</sup>, and this value is even lower than that of CG-TiO<sub>2</sub>. Finally, the long-term cycling stability at high current density (0.4 A g<sup>-1</sup>) for CG-TiO<sub>2</sub>@C, CG-TiO<sub>2</sub> and A600 is reported Fig. 7f. After 100 cycles, CG-TiO<sub>2</sub>@C retains 73 % of its initial capacity with a coulombic efficiency of more than 99.7 %, remarkably better than CG-TiO<sub>2</sub> or A600, which show retentions of 52 % and 65 %, respectively. This result suggests that the carbon matrix of CG-TiO<sub>2</sub>@C stabilises TiO<sub>2</sub> particles, and confirms that the properties of carbon matrix of CG-TiO<sub>2</sub>@C are different from those of A600. These results hint that this carbon matrix of CG-TiO<sub>2</sub>@C can effectively improve the electronic conductivity of the composite. To evaluate the influence of the carbon matrix on the electronic conductivity of the composite, CG-TiO<sub>2</sub>@C and CG-TiO<sub>2</sub> electrodes without carbon black additive (CB) were also tested. Interestingly, CG-TiO<sub>2</sub>@C without CB electrode delivered 453 mAh g<sup>-1</sup> as 2<sup>nd</sup> discharge capacity, even higher than that of A600 with CB, whereas a capacity of only 25 mAh g<sup>-1</sup> was recorded for CG-TiO<sub>2</sub> without CB (Fig. S8).

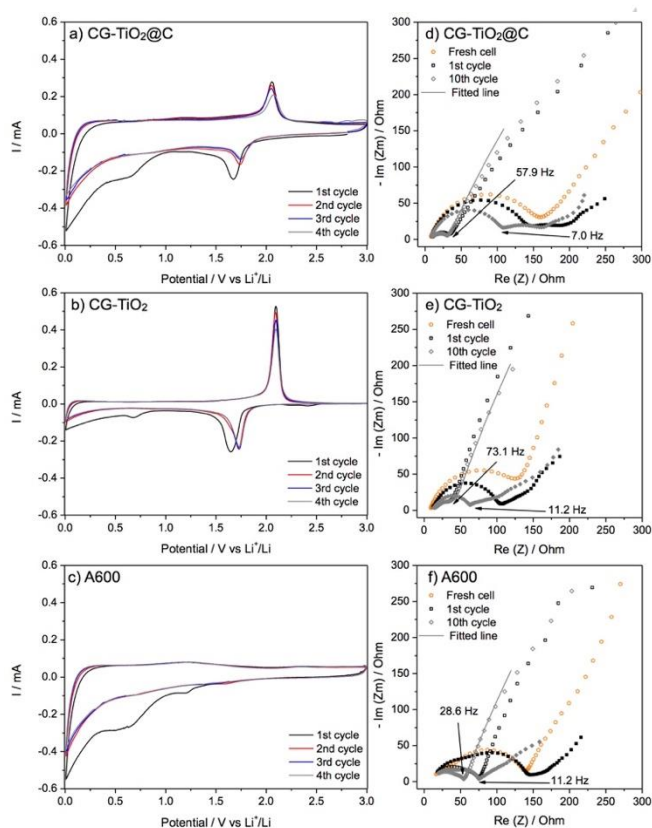


**Fig. 8.** CV curves at a scan rate of 0.1 mV s<sup>-1</sup> for a) CG-TiO<sub>2</sub>@C, b) CG-TiO<sub>2</sub>, c) A600 and d-f) their Nyquist plots; filled and open symbols refer to the end of discharge (0.01V) and the end of charge (3.0V), respectively.

To better understand the improved electrochemical performance of CG-TiO<sub>2</sub>@C compared to CG-TiO<sub>2</sub> and A600, cyclic voltammetry (CV) was performed at a scan rate of 0.1 mV s<sup>-1</sup> within the 0.01 - 3.0 V (vs Li<sup>+</sup>/Li) voltage range. As shown in Fig. 8b, GC-TiO<sub>2</sub> presents a typical CV curve of anatase with a cathodic/anodic peak pair around 1.7/2.0 V, corresponding to the insertion/disinsertion of lithium in TiO<sub>2</sub>. No additional peaks are observed below 1.0 V, confirming that the lithium storage process mainly arises from the contribution of TiO<sub>2</sub>. A small cathodic peak at 0.7 V, recorded only during the first cycle, is attributed to the decomposition of electrolyte on the surface of the electrode. In case of mesoporous carbonaceous material A600 (Fig. 8c), the two cathodic peaks at 1.4 V and 0.7 V during the first cycle are probably due to irreversible reactions such as the reaction of lithium with oxygenated surface groups in A600 (1.4 V) and the decomposition of electrolyte (0.7 V), resulting in the formation of the SEI.<sup>[59]</sup> These two peaks are not observed during the following cycles, leaving only a peak at 0.1 V associated with the reversible insertion of lithium in amorphous carbon. From the second cycle onwards, CV curves are almost identical, confirming that the structure of A600 and the SEI formed at its surface are stable, without any significant degradation during cycling.

As it could be considered as a hybrid material of CG-TiO<sub>2</sub> and A600, CG-TiO<sub>2</sub>@C exhibits a complex CV profile, which can be separated into two contributions: one typical of TiO<sub>2</sub> and one resembling that of A600. The cathodic/anodic peaks pair of the TiO<sub>2</sub> contribution is obviously less intense than that of CG-TiO<sub>2</sub>, due to the small content of TiO<sub>2</sub> (76 wt%) in the composite. Only one irreversible peak, less pronounced than in A600, is observed at 0.7 V during the first cycle. In addition, the peak at 1.4 V, previously attributed to the possible reaction of lithium with oxygenated groups at the surface of carbon, is not visible. These differences in the CV profiles of CG-TiO<sub>2</sub>@C and A600, confirm the different properties of the carbon in the two samples. This difference positively impacts the electrochemical performance of CG-TiO<sub>2</sub>@C, increasing its specific capacity.

To understand the performance in CG-TiO<sub>2</sub>@C, compared to A600, cyclic voltammetry at different scan rates (0.1 mV to 10 mV s<sup>-1</sup>) was performed (Fig. 9) Briefly, for lithium storage in carbonaceous material, the total capacity can be divided into a faradaic contribution (e.g., formation of the SEI and lithium intercalation) and a non-faradaic one (e.g., capacitive charge). In order to estimate the extent of these two contributions, the cyclic voltammetry curves at different scan rates from 0 to 1.0 V were analyzed following equation (1):<sup>[64]</sup>

$$i = av^b \quad (1)$$

where  $i$  is the current,  $v$  the scan rate and  $a$ ,  $b$  are adjustable parameters which can be determined empirically by plotting  $\log i$  vs  $\log v$ . For a non-faradaic capacitive charge mechanism,  $b$  approaches 1.0, whereas this parameter is close to 0.5 for a mostly faradaic mechanism.<sup>[65],[66]</sup> For CG-TiO<sub>2</sub>@C,  $b$  takes values between 0.65 and 0.7, indicating a dominant faradaic contribution. For A600, on the contrary,  $b$  increases from 0.65 to 0.82 suggesting a more capacitive charge mechanism. In summary, the carbon matrix of CG-TiO<sub>2</sub>@C show typical 'carbon-like' insertion properties (with C:O ratio of 23.7), whereas the non-



negligible oxygenated functional groups (C:O ratio of 14.0) in A600 might favour a non-faradaic capacitive charge process. Given the interesting results CG-TiO<sub>2</sub>@C, electrochemical impedance spectroscopy (EIS) analysis was carried at different depths-of-discharge during cycling, and the corresponding Nyquist plots are presented in Fig. 8d-f. At the end of the first discharge (0.01 V, insertion of lithium), CG-TiO<sub>2</sub> shows a depressed single semicircle at high frequency region, which can be associated, as usual, with the charge transfer process ( $R_{ct}$ ) and the solid electrolyte interphase ( $R_{SEI}$ ).

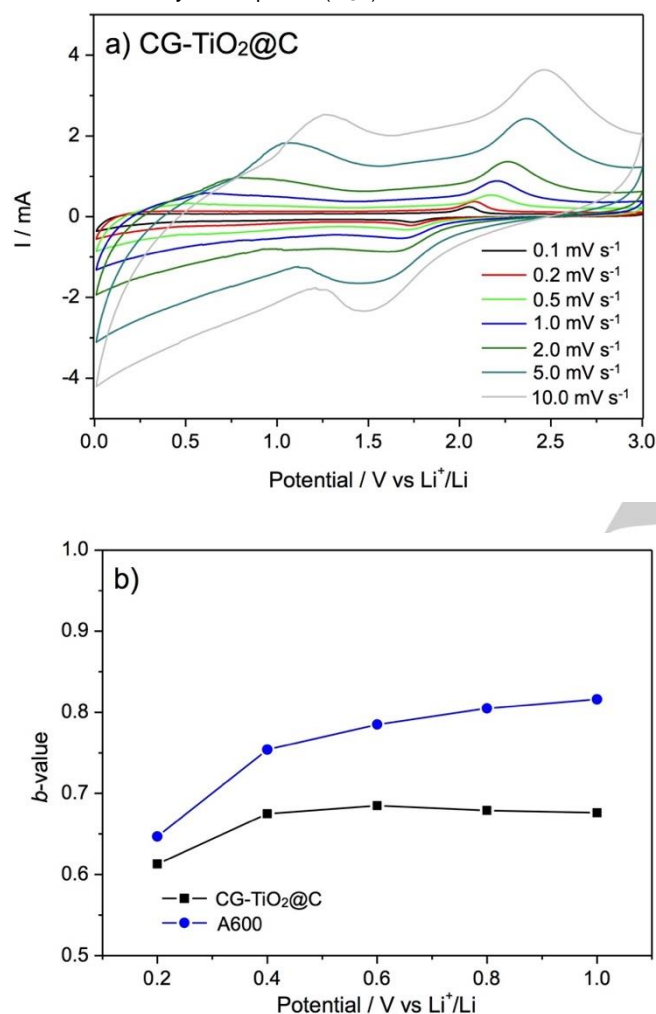


**Fig. 9.** a) CV curves of CG-TiO<sub>2</sub>@C electrode at various scan rates (2nd cycle), from 0.1 mV s<sup>-1</sup> to 10.0 mV s<sup>-1</sup>, b) Calculated b-values for CG-TiO<sub>2</sub>@C and A600 electrodes as a function of the cathodic (lithium insertion) sweep.

On the contrary, the Nyquist plot of CG-TiO<sub>2</sub>@C exhibits an additional depressed semicircular arc at medium frequency, which should be related to semi-infinite diffusion-like processes as often observed in hard carbon materials.<sup>[67]</sup> However, the appearance of this semicircular is very different from that of A600, suggesting again that the carbon matrix in CG-TiO<sub>2</sub>@C is not the same as A600. The Nyquist plots recorded at the end of the charge (3.0 V, disinsertion of lithium) both CG-TiO<sub>2</sub> and CG-TiO<sub>2</sub>@C show a similar feature with a single semicircle at high

frequency region, and the semicircle of CG-TiO<sub>2</sub>@C is slightly smaller than that of CG-TiO<sub>2</sub> ( $R_{ct}$  of 24.1 Ohm vs 32.8 Ohm). At this state, as all lithium ions are removed from the electrode, no signature of resistance related to lithiated carbon is observed for CG-TiO<sub>2</sub>@C. Therefore, it can be deduced that the carbon content in CG-TiO<sub>2</sub>@C may now effectively improve the electronic conductivity, thus ensuring a faster interfacial charge transfer. In addition, CG-TiO<sub>2</sub>@C shows smaller Warburg diffusion impedance,  $\sigma$  (See Table S2 and Fig. S9 for fitting results), compared to CG-TiO<sub>2</sub> and A600, which could imply that carbon matrix of CG-TiO<sub>2</sub> enhances the lithium ion diffusion process. Indeed, the presence of carbon could increase the number of electron-conducting pathways,<sup>[68]</sup> especially when the carbon is homogeneously dispersed as a composite with active material (CG-TiO<sub>2</sub>@C). Notably, the resistivity of CG-TiO<sub>2</sub>@C at charged state is almost identical with cycling, giving the same semicircle feature, indicating the excellent stability of the electrode.

## Conclusions

This work presents a new concept in the use of alginic acid for the elaboration of metal oxides and metal oxide/carbon composites, with positive influence on the performance of these materials as anodes in LiBs. Indeed, beside the classical use of this biopolymer as template of metal oxide, it is also used here for the first time as a reagent and as a source of O and C atoms. The present methodology of preparation of mesoporous TiO<sub>2</sub>@C nanocomposites, based on the reactivity of alginic acid towards metal chloride, is among the greenest possible way in terms of economy of atoms, solvent, energy and equipment. Above all, it leads to high performance materials that, although not optimized, show a great potential for energy applications. Thanks to the synergy between the aerogel structure, the effect of the metal chloride treatment and the pyrolysis step, mesoporous TiO<sub>2</sub>@C nanocomposite shows a high capacity due to the electrochemical active role of the carbon matrix and an improved capacity retention even at high rates (up to 1.2 A g<sup>-1</sup>).

This concept can be probably generalised to other polysaccharide aerogels and/or other metal oxides making it a new broad scope and Green approach for the elaboration of materials for energy storage and catalysis.

## Experimental Section

**Chemicals.** Alginic acid powder (AA-P) from brown algae was purchased from Sigma-Aldrich (France). Titanium(IV) chloride (TC, TiCl<sub>4</sub>, >99.9%) and tert-butyl alcohol (TBA, C<sub>4</sub>H<sub>10</sub>O, >99.5%) were purchased from ACROS (France). Super P (>99%) was purchased from Alfa Aesar (France). All reagents were used without further purification.

**Synthesis of mesoporous alginic acid cryogel.** A mesoporous cryogel of alginic acid was prepared as reported previously.<sup>[65]</sup> Briefly, an alginic acid solution (4.8 wt% in water) was gelled by heating at 90 °C for 2.5 h, and then kept at 4 °C for 24 h for retrogradation of alginic acid. Afterwards, tert-butyl alcohol (TBA) was added to the alginic acid gel, to obtain the eutectic composition of water and TBA (weight ratio of 7:3). The mixture

## FULL PAPER

was stirred for 1 h at RT then kept at 4 °C for 24 h. Removal of solvent by freeze drying was performed - 85 °C under 50 mbar, giving the mesoporous cryogel of alginic acid GC.

**Synthesis of mesoporous TiO<sub>2</sub>, TiO<sub>2</sub>@C composite, and A600 materials.** In a glove box, an alginic acid cryogel (0.352 g, 2.0 mmol) and a pure titanium(IV) chloride (1.138 g, 6.0 mmol) were introduced in the Teflon liner of a steel autoclave, and then kept in an oven at 80 °C for 3 days under autogenous pressure. After cooling and eventually washing with ethanol (3 × 20 mL), the obtained mesoporous TiO<sub>2</sub>@CG was further dried at 80 °C for 12 h under vacuum. Mesoporous TiO<sub>2</sub> (CG-TiO<sub>2</sub>) was obtained by calcination of TiO<sub>2</sub>@CG at 600 °C in air (1 °C min<sup>-1</sup>, 5 h at 600 °C). Mesoporous TiO<sub>2</sub>@C (CG-TiO<sub>2</sub>@C) was obtained by pyrolysis of TiO<sub>2</sub>@CG at 600 °C in argon flow inside a tubular furnace (1 °C min<sup>-1</sup>, 5 h at 600 °C, 150 mL min<sup>-1</sup> of argon flow). For the synthesis of non-porous TiO<sub>2</sub> (P-TiO<sub>2</sub>) or TiO<sub>2</sub>@C (P-TiO<sub>2</sub>@C), alginic acid powder (P) was introduced in the autoclave and treated in the same conditions than CG and the resulting hybrid TiO<sub>2</sub>@AAP was converted by pyrolysis or calcination in same condition. Besides, a mesoporous carbonaceous material derived from alginic acid (A600) was prepared by the direct carbonization of the alginic acid cryogel at 600 °C under argon flow in a tubular furnace (1 °C min<sup>-1</sup>, 5 h at 600 °C, 150 mL min<sup>-1</sup> of argon flow).

**Characterization.** Powder X-ray diffraction (XRD) patterns were measured using a PANalytical X'Pert Pro MPD diffractometer, equipped with Cu K $\alpha$  radiation (1.5418 Å), in the 10 - 80° 2 $\theta$  range with steps of 0.033°. N<sub>2</sub> physisorption experiments were carried out at -196 °C on a Micromeritics 3Flex. The samples were outgassed at 120 °C for 10 h at 10<sup>-3</sup> mbar before the analysis. Scanning electron microscopy (SEM) images were obtained on a Hitachi S-4800 electron microscope. Energy-dispersive X-ray spectroscopy (EDX) analyses were acquired with a JEOL CENTURIO detector. Transmission electron microscopy (TEM) and Scanning Transmission electron microscopy (STEM) images were acquired using JEOL FX2200 microscope. <sup>13</sup>C CP/MAS NMR spectra were recorded on a VARIAN VNMRs 300 MHz spectrometer using a 3.2 mm T 3 2 channels probe. Rotors were spun at 12 kHz. Energy-dispersive X-ray spectroscopy (EDX) analyses were acquired with a JEOL CENTURIO detector. Raman spectra were measured on a Horiba Jobin-Yvon LabRAM ARAMIS microspectrometer with the excitation wavelength was 633 nm. TG analyses were performed using Netzsch Simultaneous Thermal Analyser STA 409 PC Luxx system. Galvanostatic electrochemical characterizations were performed at RT on a BTS3000 instrument (Neware Battery). Electrochemical impedance spectroscopy (EIS) studies were done on a VSP-300 (BioLogic), from 100 kHz to 10 mHz, with a 10 mV amplitude in the potentiostatic mode. Cyclic voltammetry (CV) measurements were carried out on a VSP-300 (BioLogic) with scan rate of 0.1 mV s<sup>-1</sup>. The electrodes are composed of the active material, a conductive carbon additive (Super P), and polyvinylidene fluoride (PVDF, Solef 5130) in the mass ratio of 80:14:6. After stirring in N-methyl-2-pyrrolidone (NMP, Sigma-Aldrich), the electrode slurry was mixed in an agate grinding jar (1 h at 500 rpm), then tape casted uniformly at 150 mm onto a copper current collector (0.018 mm, 99.96%, Promotor) using a 3540 bird film applicator (Elcometer). Electrodes were cut out from the film (diameter of 12.7 mm) and dried under vacuum at 80 °C for 15 h. The tap density of the electrodes was ca. 1.8 mg cm<sup>-2</sup>. CR2032 coin-type cells were assembled in a glove box (Braun) under Ar atmosphere (O<sub>2</sub> < 0.5 ppm, H<sub>2</sub>O < 0.5 ppm), using lithium metal as both reference and counter electrode. The electrolyte was LP30 (1M LiPF<sub>6</sub> in ethylene carbonate (EC) and dimethyl carbonate (DMC) (v/v = 1:1)). Whatman glass fibre disks were used as separators. Electrochemical galvanostatic cycling was performed in the voltage window 3.00 - 0.01 V vs Li<sup>+</sup>/Li at several different current densities.

## Author Contribution

SK synthesized all electrode materials and carried out electrochemical testing and analysis. MD synthesized the cryogel of alginic acid with advice from DJM. JGA, NL, NB, LS, PHM supervised data analysis. SK and BB wrote the manuscript with advice from LS and LM. LM and BB oversaw the study. All authors discussed the results and commented on the manuscript.

## Acknowledgements

Financial support was received from the European Commission in the framework of POROUS4APP project (H2020 GA no. 666157). The authors would like to thank Didier Cot, Bertrand Rebiere (IEM, France) for SEM analysis, and Erwan Oliviero (Université de Montpellier, France) for TEM analysis. Lea Daenens (ICGM, France) is gratefully acknowledged for technical help in the collection of the Raman spectra.

**Keywords:** Cryogel, alginic acid, TiO<sub>2</sub>, mesoporous, lithium ion battery

- [1] M. Armand and J. M. Tarascon, *Nature*, **2008**, 451, 652–657.
- [2] V. Etacheri, R. Marom, R. Elazari, G. Salitra and D. Aurbach, *Energy Environ. Sci.*, **2011**, 4, 3243–20.
- [3] B. Boury and S. Plumejeau, *Green Chem.*, **2015**, 17, 72–88.
- [4] J. Jiang, Y. Li, J. Liu, X. Huang, C. Yuan and X. W. D. Lou, *Adv. Mater.*, **2012**, 24, 5166–5180.
- [5] A. Henry, P. Hesemann, J. G. Alauzun and B. Boury, *Carbohydr. Polym.*, **2017**, 174, 697–705.
- [6] X. Cao, C. Tan, M. Sindoro and H. Zhang, *Chem. Soc. Rev.*, **2017**, 46, 2660–2677.
- [7] R. Wu, X. Qian, K. Zhou, J. Wei, J. Lou and P. M. Ajayan, *ACS Nano*, **2014**, 8, 6297–6303.
- [8] X. Han, Z. Zhao, Y. Xu, D. Liu, H. Zhang and C. Zhao, *RSC Adv.*, **2014**, 4, 41968–41975.
- [9] Q. Li, X. Miao, C. Wang and L. Yin, *J. Mater. Chem. A*, **2015**, 3, 21328–21336.
- [10] X. Li, H. Hu, S. Huang, G. Yu, L. Gao, H. Liu and Y. Yu, *Electrochim. Acta*, **2013**, 112, 356–363.
- [11] S. Kim, J. G. Alauzun, N. Louvain, N. Brun, L. Stievano, B. Boury, L. Monconduit and P. H. Mutin, *RSC Adv.*, **2018**, 8, 32558–32564.
- [12] E. Zhao, C. Qin, H.-R. Jung, G. Berdichevsky, A. Nese, S. Marder and G. Yushin, *ACS Nano*, **2016**, 10, 3977–3984.
- [13] A. S. Aricò, P. Bruce, B. Scrosati and J. M. Tarascon, *Nat. Mater.*, **2005**, 4, 366–377.
- [14] P. G. Bruce, B. Scrosati and J.-M. Tarascon, *Angew. Chem. Int. Ed.*, **2008**, 47, 2930–2946.
- [15] S. Spirk, *Polysaccharides as Battery Components*, Springer International Publishing, Cham, **2018**.
- [16] S. Kim, M. De Bruyn, J. G. Alauzun, N. Louvain, N. Brun, D. J. Macquarrie, L. Stievano, B. Boury, L. Monconduit and P. H. Mutin, *J. Mater. Chem. A*, **2018**, 6, 14392–14399.
- [17] A. Henry, S. Plumejeau, L. Heux, N. Louvain, L. Monconduit, L. Stievano and B. Boury, *ACS Appl. Mater. Interfaces*, **2015**, 7, 14584–14592.
- [18] A. Henry, N. Louvain, O. Fontaine, L. Stievano, L. Monconduit and B. Boury, *ChemSusChem*, **2016**, 9, 264–273.
- [19] T. Meng, R. Zeng, Z. Sun, F. Yi, D. Shu, K. Li, S. Li, F. Zhang, H. Cheng and C. He, *J. Electrochem. Soc.*, **2018**, 165, A1046–A1053.

- [20] W. Li, L. Li, X. Wu, J. Li, L. Jiang, H. Yang, G. Ke, G. Cao, B. Deng and W. Xu, *ACS Appl. Mater. Interfaces*, **2018**, 10, 21056–21060.
- [21] M. Kemell, V. Pore, M. Ritala and M. Leskelä, *Chem. Vap. Deposition*, **2006**, 12, 419–422.
- [22] Z. Li, C. Yao, Y.-C. Wang, S. Mikael, S. Gunasekaran, Z. Ma, Z. Cai and X. Wang, *J. Mater. Chem. A*, **2016**, 4, 11672–11679.
- [23] M. Kettunen, R. J. Silvennoinen, N. Houbenov, A. Nykänen, J. Ruokolainen, J. Sainio, V. Pore, M. Kemell, M. Ankerfors, T. Lindström, M. Ritala, R. H. A. Ras and O. Ikkala, *Adv. Funct. Mater.*, **2010**, 21, 510–517.
- [24] H. Ghanem, M. Kormann, H. Gerhard and N. Popovska, *J. Eur. Ceram. Soc.*, **2007**, 27, 3433–3438.
- [25] M. L. Foresti, A. Vázquez and B. Boury, *Carbohydr. Polym.*, **2017**, 157, 447–467.
- [26] S. Li and J. Huang, *Adv. Mater.*, **2015**, 28, 1143–1158.
- [27] H. Tian and J. He, *Langmuir*, **2016**, 32, 12269–12282.
- [28] E. Hermann, *Extreme Biomimetics*, Springer, 2017.
- [29] A. A. Makarova, E. V. Grachova, V. S. Neudachina, L. V. Yashina, A. Blüher, S. L. Molodtsov, M. Mertig, H. Ehrlich, V. K. Adamchuk, C. Laubschat, D. V. Vyalykh, *Sci. Rep.*, **2015**, 5, 8710.
- [30] H. Ehrlich, P. Simon, M. Motylenko, M. Wysokowski, V. V. Bazhenov, R. Galli, A. L. Stelling, D. Stawski, M. Ilan, H. Stöcker, B. Abendroth, R. Born, T. Jesionowski, K. J. Kurzydłowski, D. C. Meyer, *J. Mater. Chem. B*, **2013**, 1, 5092–5099.
- [31] M. Wysokowski, I. Petrenko, A. L. Stelling, D. Stawski, T. I. Jesionowski, H. Ehrlich, *Polymers*, **2015**, 7, 235–265.
- [32] I. Stepniak, M. Galinski, K. Nowacki, M. Wysokowski, P. Jakubowska, V. V. Bazhenov, T. Leisegang, H. Ehrlich, T. Jesionowski, *RSC Adv.*, **2016**, 6, 4007–4013.
- [33] T. Szatkowski, K. Kopczyński, M. Motylenko, H. Borrmann, B. Mania, M. Graś, G. Lota, V. V. Bazhenov, D. Rafaja, F. Roth, J. Weise, E. Langer, M. Wysokowski, S. Żółtowska-Aksamitowska, I. Petrenko, S. L. Molodtsov, J. Hubáľková, C. G. Aneziris, Y. Joseph, A. L. Stelling, H. Ehrlich, T. Jesionowski, *Nano Res.*, **2018**, 11, 4199.
- [34] T. Szatkowski, K. Siwińska-Stefańska, M. Wysokowski, A. L. Stelling, Y. Joseph, H. Ehrlich, T. Jesionowski, *Biomimetics*, **2017**, 2, 4.
- [35] S. Li, J. Huang, *J. Mater. Chem. A*, **2015**, 3, 4354–4360.
- [36] Y. Luo, J. Li, J. Huang, *Langmuir*, **2016**, 32, 12338–12343.
- [37] M. Wang, S. Li, Y. Zhang, J. Huang, *Chem. Eur. J.*, **2015**, 21, 16195–16202.
- [38] S. Behar, P. Gonzalez, P. Agulhon, F. Quignard, D. Swierczynski, *Catal. Today*, **2012**, 189, 35–41.
- [39] E. Wan, A. Travert, F. Quignard, D. Tichit, N. Tanchoux, H. Petitjean, Hugo, *ChemCatChem*, **2017**, 9, 2358–2365.
- [40] A. M. Escamilla-Pérez, N. Louvain, M. Kaschowitz, S. Freunberger, O. Fontaine, B. Boury, N. Brun and P. H. Mutin, *J. Sol-Gel Sci. Technol.*, **2017**, 79, 270–278.
- [41] A. Henry, N. Louvain, O. Fontaine, L. Stievano, L. Monconduit and B. Boury, *ChemSusChem*, **2016**, 9, 264–273.
- [42] S. Plumejeau, M. Rivallin, S. Brosillon, A. Ayrat, L. Heux and B. Boury, *Chem. Eur. J.*, **2016**, 22, 17262–17268.
- [43] S. Plumejeau, M. Rivallin, S. Brosillon, A. Ayrat and B. Boury, *Eur. J. Inorg. Chem.*, **2016**, 1200–1205.
- [44] S. Kim, A. M. Escamilla-Pérez, M. De Bruyn, J. G. Alauzun, N. Louvain, N. Brun, D. J. Macquarrie, L. Stievano, B. Boury, L. Monconduit and P. H. Mutin, *J. Mater. Chem. A*, **2017**, 5, 24380–24387.
- [45] A. R. Armstrong, G. Armstrong, J. Canales, R. García and P. G. Bruce, *Adv. Mater.*, **2005**, 17, 862–865.
- [46] G. Sudant, E. Baudrin, D. Larcher and J.-M. Tarascon, *J. Mater. Chem.*, **2005**, 15, 1–7.
- [47] A. M. Escamilla-Pérez, N. Louvain, B. Boury, N. Brun and P. H. Mutin, *Chem. Eur. J.*, **2018**, 24, 4982–4990.
- [48] H. Liu, W. Li, D. Shen, D. Zhao and G. Wang, *J. Am. Chem. Soc.*, **2015**, 137, 13161–13166.
- [49] M. Fehse, S. Cavaliere, P. E. Lippens, I. Savych, A. Iadecola, L. Monconduit, D. J. Jones, J. Rozière, F. Fischer, C. Tessier and L. Stievano, *J. Phys. Chem. C*, **2013**, 117, 13827–13835.
- [50] H.-G. Jung, C. S. Yoon, J. Prakash and Y.-K. Sun, *J. Phys. Chem. C*, **2009**, 113, 21258–21263.
- [51] J.-Y. Shin, D. Samuelis and J. Maier, *Adv. Funct. Mater.*, **2011**, 21, 3464–3472.
- [52] M. Zou, Z. Ma, Q. Wang, Y. Yang, S. Wu, L. Yang, S. Hu, W. Xu, P. Han, R. Zou and A. Cao, *J. Mater. Chem. A*, **2016**, 4, 7398–7405.
- [53] L. Sun, W. Liu, Y. Cui, Y. Zhang, H. Wang, S. Liu, B. Shan, *Green Chem.*, **2018**, 20, 3954–3962.
- [54] L. Zheng, X. Wang, Y. Xia, S. Xia, E. Metwalli, B. Qiu, Q. Ji, S. Yin, S. Xie, K. Fang, S. Liang, M. Wang, X. Zuo, Y. Xiao, Z. Liu, J. Zhu, P. Müller-Buschbaum and Y.-J. Cheng, *ACS Appl. Mater. Interfaces*, **2018**, 10, 2591–2602.
- [55] A. Borisova, M. De Bruyn, V. L. Budarin, P. S. Shuttleworth, J. R. Dodson, M. L. Segatto and J. H. Clark, *Macromol. Rapid Commun.*, **2015**, 36, 774–779.
- [56] J. P. Soares, J. E. Santos, G. O. Chierice and E. T. G. Cavalheiro, *Ecl. Quím., São Paulo*, 2004, 29, 53–56.
- [57] C. M. DeRamos, A. E. Irwin, J. L. Nauss and B. E. Stout, *Inorg. Chim. Acta.*, **1997**, 256, 69–75.
- [58] P. H. Mutin and A. Vioux, *Chem. Mater.*, 2009, 21, 582–596.
- [59] S. Kim, M. De Bruyn, J. G. Alauzun, N. Louvain, N. Brun, D. J. Macquarrie, L. Stievano, B. Boury, P. H. Mutin and L. Monconduit, *J. Power Sources*, **2018**, 406, 18–25.
- [60] W. F. Zhang, Y. L. He, M. S. Zhang, Z. Yin and Q. Chen, *J. Phys. D: Appl. Phys.*, **2000**, 33, 912–916.
- [61] D. Chen, L. Zou, S. Li and F. Zheng, *Sci. Rep.*, **2018**, 1–8.
- [62] A. W. Czanderna, C. N. Ramachandra Rao, J. M. Honig, *Trans. Faraday Soc.*, **1958**, 54, 1069–1073.
- [63] S. Patra, C. Davoisne, H. Bouyanfif, D. Foix, F. Sauvage, *Sci. Rep.*, **2015**, 5, 10928.
- [64] Y. Wang, Y. Song and Y. Xia, *Chem. Soc. Rev.*, **2016**, 45, 5925–5950.
- [65] T. Brezesinski, J. Wang, S. H. Tolbert and B. Dunn, *Nat. Mater.*, **2010**, 9, 146–151.
- [66] A. J. Bard, L. R. Faulkner, *Electrochemical Methods: Fundamentals and Applications*, second ed., John Wiley & Sons, **2000**.
- [67] R. Väli, A. Jänes and E. Lust, *J. Electrochem. Soc.*, **2017**, 164, E3429–E3437.
- [68] J. H. Jeong, M.-S. Kim, Y. J. Choi, G.-W. Lee, B. H. Park, S.-W. Lee, K. C. Roh and K.-B. Kim, *J. Mater. Chem. A*, **2018**, 6, 6033–6044.



## FULL PAPER

Entry for the Table of Contents (Please choose one layout)

## FULL PAPER



Sanghoon Kim, Mario De bruyn, Johan G. Alauzun, Nicolas Louvain, Nicolas Brun, Duncan J. Macquarrie, Lorenzo Stievano, P. Hubert Mutin, Laure Monconduit,\* and Bruno Boury\*

**Page No. – Page No.**

Simple and eco-friendly method for a direct conversion of seaweed into mesoporous TiO<sub>2</sub>@C was developed with application for lithium ion battery.

**Dehydration of alginic acid cryogel by TiCl<sub>4</sub> vapor: a direct access to mesoporous TiO<sub>2</sub>@C nanocomposites and their performance in lithium ion batteries**